Astronomy & Astrophysics manuscript no. aa37336-19
September 30, 2021
©ESO 2021

Are observed H I filaments turbulent illusions or density structures?

Velocity caustics: facts and fakes

P. M. W. Kalberla[1] and U. Haud[2]

[1] Argelander-Institut für Astronomie, Auf dem Hügel 71, 53121 Bonn, Germany
e-mail: pkalberla@astro.uni-bonn.de
[2] Tartu Observatory, University of Tartu, 61602 Tõravere, Tartumaa, Estonia

Received 17 December 2019 / Accepted 21 April 2020

arXiv:2003.01454v2 [astro-ph.GA] 2 Jan 2021

ABSTRACT

Context. The interstellar medium is affected by turbulence, and observed H I structures in channel maps are shaped by turbulent motions. It is taken for granted by a few theoreticians that observed H I structures do not represent real density enhancement, rather velocity caustics caused by velocity crowding. This interpretation has been questioned, and the objections have led to heated debates.
Aims. To settle the discussion we verify theoretical key parameters by using the Effelsberg Bonn H I Survey (EBHIS) observations.
Methods. We apply unsharp masking to determine filamentary H I structures at high spatial frequencies. In addition we use Gaussian parameters to distinguish the cold neutral medium (CNM) from observed H I column densities. We compare power spectra and spatial distributions of dust and H I column densities in order to distinguish CNM and multiphase column densities at various velocity widths.
Results. Observations contradict the Velocity Channel Analysis (VCA) postulate that the spectral index should steepen with the width of the velocity window. We instead find that the thin slice spectral index depends strongly on the H I phase composition. Multiphase power spectra are steeper for regions with cold gas. VCA contradicts such H I phase dependences on the power distribution. Separating the CNM we find that the power spectra are significantly flatter than those for the multiphase H I composite. We observe excess CNM power for small-scale structures originating from cold dust-bearing filaments that are embedded in the CNM. Spectral indices for narrow channel widths depend on the Doppler temperature of the H I gas. In the presence of enhanced small-scale H I structure the far-infrared emission from dust is also enhanced.
Conclusions. Small-scale cold filamentary H I structures are predominantly caused by density enhancements due to phase transitions rather than by velocity caustics.

Key words. Turbulence – ISM: clouds – ISM: structure – (ISM:) dust,extinction

1. Introduction

Density distribution and motion of the interstellar medium (ISM) are affected by many factors, most notably Galactic dynamics, but it has also been suggested that turbulence is important for all ISM constituents on all scales (Armstrong et al. 1995). The ISM contains ionized, molecular, and atomic components; here we are concerned with the neutral hydrogen (H I) which fills a large fraction of the Milky Way disk and halo. H I is easily observable and is therefore an ideal tracer for various ISM structures. All-sky surveys, like the combined Effelsberg and Parkes H I survey (HI4PI, HI4PI Collaboration et al. 2016) or the Galactic Arecibo L-Band Feed Array Survey (GALFA-H I, Peek et al. 2018), disclose a wealth of structures in data cubes that are organized in channel maps with position-position-velocity (PPV) coordinates. Comparing the new high resolution surveys with the older low resolution Leiden-Argentine-Bonn (LAB) data (Kalberla et al. 2005), we find that the new data contain a striking wealth of previously unknown filamentary H I structures that are aligned with the magnetic field and correlated with far-infrared (FIR) emission observed by *Planck*, see Clark et al. (2014, 2015), Kalberla et al. (2016), Peek et al. (2018), Clark et al. (2019), and Clark, & Hensley (2019). The access to the H I survey data is easy, but the interpretation is hampered by the fact that these data do not contain the full 3D phase space information. They offer only projections with information for two perpendicular spatial coordinates and a single one along the line of sight in velocity.

Restrictions for the turbulence analysis of such PPV data have been considered by Lazarian & Pogosyan (2000) for an isothermal medium under the assumption that the velocity field is uncorrelated with the density field. They have argued that 3D power laws for the density field derived from PPV column density maps should depend on the width of the velocity slice used. Intensity fluctuations in thin velocity slices are affected by both density and velocity fluctuations. In particular, when the density spectrum is long-wave dominated, the H I intensity spectrum does not reflect the density statistics. However, in the limit of very thick slices the velocity effects on the projected intensity distribution integrate out. Lazarian & Pogosyan (2000) suggest that the velocity fluctuations for thin slices make the spectra of emissivity more shallow, which creates many structures in position-position-velocity (PPV) space that might be identified as clouds (see their Sect. 7). Such spurious structures are be caused by velocity crowding along the line of sight and are called velocity caustics. Lazarian & Yuen (2018) claim that filamentary structures in thin channel maps, mentioned in the previous paragraph and discussed in detail by Clark et al. (2014,

2015), are predominantly velocity caustics, thus not real but an illusion caused by turbulence.

Clark et al. (2019) object against this interpretation. They consider the spatial correlation between small-scale H I filaments and *Planck* 857 GHz emission (Planck 2018 results. IV. 2018) as an indication that filamentary H I structures are true density structures in the ISM. From the fact that the best FIR–H I correlation as well as the highest FIR-to-H I ratio is found for cold filamentary H I structures, they infer that the enhanced FIR emission is associated with colder, denser phases of the ISM. Thus, structures must be caused by dust-bearing density structures and not by velocity caustics. The anisotropic cold H I structures are most obvious in thin velocity slices and are observable at high spatial frequencies. Such H I features are washed out in thick velocity slices where structures are dominated by the more extended and isotropic WNM. Changes in spectral slope are attributed to changes in the multiphase composition of the H I rather than to velocity fluctuations. Clark et al. (2019) conclude that thin slice spectral indices must be affected by "small-scale structure and narrow line widths typical of CNM" and call for "a significant reassessment of many observational and theoretical studies of turbulence in H I."

Yuen et al. (2019) comment on Clark et al. (2019), and argue that thin channels always have a contribution from velocity fluctuations. They note that the "most valuable insight from Lazarian & Pogosyan (2000) is the prediction of the spectral slope change between the thin and thick PPV slices that is related to the spectral indices of turbulent velocity and density." This is in fact the heart of the velocity channel analysis (VCA). The theory was extensively tested with numerical data; we refer to references given by Yuen et al. (2019). VCA was formulated for the isothermal gas, but Yuen et al. (2019) argue further that temperature inhomogeneities would increase the weight of velocity related contributions to the velocity channel map, keeping the VCA phenomenon of spectral slope transitions intact. They claim that two-phase medium and one-phase medium both show the same result. They question further that the H I filaments are indicative of cold gas and note that the data presented by Clark et al. (2019) are close to the North Galactic Pole where "neither formation of cold H I nor an increase of dust emissivity is likely." Last not least, Yuen et al. (2019) give counter examples for a particular region and question whether the relation between FIR emission and H I column density, derived by Clark et al. (2019), is universal.

Summing up, Clark et al. (2019) argue that filamentary H I structures that are preferentially aligned with the magnetic field and correlated with FIR emission are cold and dense, initiated by phase transitions, and thus modifying the thin velocity channel power index. Yuen et al. (2019) emphasize that temperature inhomogeneities would not affect VCA; they question whether filaments are cold, and refer to selection effects that invalidate a general correlation between FIR emission at 857 GHz and H I column density as used by Clark et al. (2019).

Putting these arguments together, we can work out three key questions: (i) Is VCA applicable to a multiphase medium with temperature inhomogeneities and embedded cold small-scale structures? (ii) How cold are H I filaments? and (iii) How close is the correlation between FIR and H I filaments?

2. Observations and data reduction

Clark et al. (2019) used Arecibo data. For a completely independent analysis we utilized here the Effelsberg Bonn H I Survey (EBHIS). We used for consistency the same region as Clark et al. (2019) and Yuen et al. (2019) and focus our analysis on a region with a diameter of 15° around longitude GAL= 35.°5 and latitude GAB= 54° (RA = $15^{d}30^{m}07^{d}$, DEC = 23°06′00″). For apodization we apply a cosine taper (a Tukey window, Harris 1978) and taper with a half-period of 15°, weighting smoothly from one to zero for a radius $15° < R < 30°$. We calculate power spectra for velocities $|v_{\rm LSR}| \leq 25$ km s^{-1} with channel widths of $\Delta v_{\rm LSR} \leq 51$ km s^{-1} in the multipole range $l < 1023$ (Kalberla & Haud 2019). To determine the small-scale spatial structure of the H I distribution at scales of $R < 0.°5$ we apply unsharp masking (USM) (Kalberla et al. 2016). The H I data are first smoothed with a Gaussian beam of 0.°5 at full width at half maximum; these smooth data are then subtracted from the original database to generate the USM data. In addition, we use a Gaussian decomposition of the HI4PI data on an nside = 1024 HEALPix grid to get parameters for different phases, and distinguish between the cold, lukewarm, and warm neutral medium (CNM, LNM, and WNM, respectively, see Kalberla & Haud (2018)).

Our methods and data processing, including deep discussions of instrumental issues, are detailed in Kalberla et al. (2016), Kalberla & Haud (2018), and Kalberla & Haud (2019). We note that the signal-to-noise ratio for the EBHIS is high enough to warrant a power analysis without a noise bias. For our extended analysis we use in general only data with a signal-to-noise ratio higher than three, corresponding to brightness temperatures $T_{\rm B} > 0.3$ K. Another major advantage of our current analysis is that we use EBHIS data alone; we do not need to consider complications in data processing related to different telescopes, as in the case of HI4PI (Kalberla & Haud 2019).

3. Power spectra

The Milky Way H I distribution differs from the simplified case of an isothermal, homogeneous, and isotropic distribution with turbulent properties that are random and uncorrelated in density and velocity, as assumed by Lazarian & Pogosyan (2000). In the first instance the column density of the observed H I depends strongly on position and radial velocity; the contributions from CNM, LNM, and WNM are then expected to vary greatly. In particular the cold part of the H I distribution, represented by the USM and CNM, tends to form filamentary structures with strong anisotropies, see Fig. 9. If the conjecture by Clark et al. (2019) against caustics is correct, we should expect an imprint of these conditions to the derived power spectra.

Figure 1 shows power spectra for EBHIS data within a single channel and for column densities integrated over $-25 < v_{\rm LSR} < 25$ km s^{-1}. In both cases the spectra are straight and well defined for $l \gtrsim 10$; the fits are also well defined with $\gamma = -2.800 \pm 0.006$ for the single channel and $\gamma = -2.879 \pm 0.006$ for the thick velocity slice. The low power for $l \lesssim 10$ reflects the limitations of our field of view with a radius of $R = 15°$, corresponding to a multipole $l \sim 180°/2R = 6$. In all cases we fit power spectra for $l \geq 10$ only.

According to VCA the spectral indices in the limits of thin and thick velocity slices determine uniquely the spectral indices of the turbulent velocity and density fields. In the case of sufficiently thick velocity slices the velocity fluctuations average out, and we measure only density fluctuations. In addition to density fluctuations, thin velocity slices also contain velocity fluctuations. These average out on large scales, hence velocity fluctuations dominate small scales and accordingly the power spectra are flattened for thin velocity slices. The difference between thin and thick slice spectral indices can then be used to determine velocity fluctuations (Yuen et al. 2019, Table 1). Taking the data

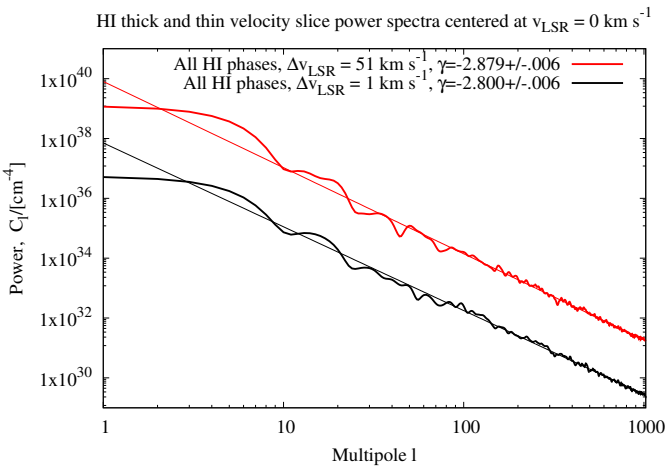


Fig. 1. Power spectra of the observed H I column density distribution at $v_{\rm LSR} = 0$ km s^{-1} for an instrumental channel width of $\Delta v_{\rm LSR} = 1.29$ km s^{-1}, corresponding to the instrumental resolution (black) and for the H I integrated in the range $-25 < v_{\rm LSR} < 25$ km s^{-1} (red). Power indices from least-squares fits for $l > 10$ are indicated; the indicated errors are formal 1σ uncertainties.

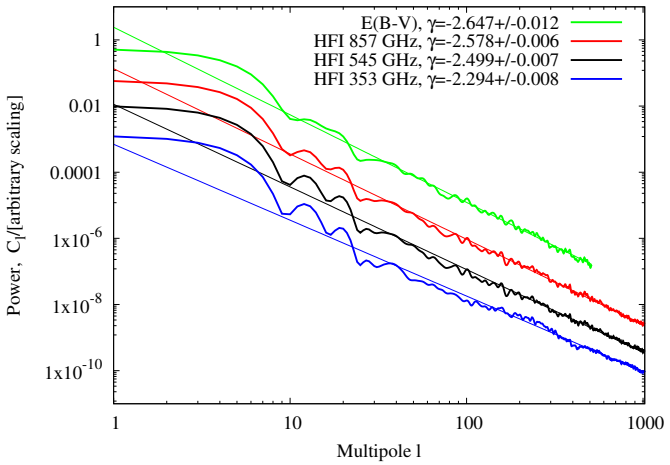


Fig. 2. Power spectra for E(B-V) and HFI emission at 857, 545, and 353 GHz with the corresponding least-squares fits.

presented in Fig. 1 at face value, we conclude that the observed spectral index γ steepens with the width of the velocity slice, as expected from theory; however, the difference $\delta\gamma_{\rm VCA} = 0.08$ is far below the expectations, indicating $m \sim 0.16$ for the slope of velocity structure function. This is only 1/4 of $m = 2/3$ that would be expected for Kolmogorov turbulence (Lazarian & Pogosyan 2000, Sect. 5.1).

Clark et al. (2019) compare H I data with *Planck* 857 GHz emission, assuming that gas and dust are well mixed. If this assumption is valid we expect that H I, FIR, and reddening power spectra are compatible. We calculate power spectra for *Planck* data at 857, 545, and 353 GHz[1]. In addition we select E(B-V) reddening data from Schlegel et al. (1998)[2]. In all cases we use the same field of view and the apodization described earlier for the H I. The power spectra, shown in Fig. 2 are calculated for $l > 10$; the E(B-V) data are only available for $l < 512$. The fits for the spectral indices show a systematical flattening with decreasing frequency, explainable by changes in the power distribution. The Galactic residual contribution to *Planck* power spectra is dominant at frequencies $\nu > 217$ GHz, the cosmic microwave background (CMB) contribution is increasing for lower frequencies, while the contribution from the cosmic infrared background (CIB) to Fig. 2 is most significant at 353 GHz (Planck intermediate results XVII. 2014, Fig. C.1). Comparing power spectra for H I with spectra for the dust distribution we note that the power spectra for the dust are well defined, but in general have significantly flatter power spectra than the observed H I column densities (Fig. 1).

[1] HFI_SkyMap_857_2048_R3.01_full.fits, HFI_SkyMap_545_2048_R3.01_full.fits, and HFI_SkyMap_353-psb_2048_R3.01_full.fits from the *Planck* Legacy Archive, https://pla.esac.esa.int/

[2] The LAMBDA Reddening (E(B-V)) Map, https://lambda.gsfc.nasa.gov/product/foreground/fg_sfd_get.cfm

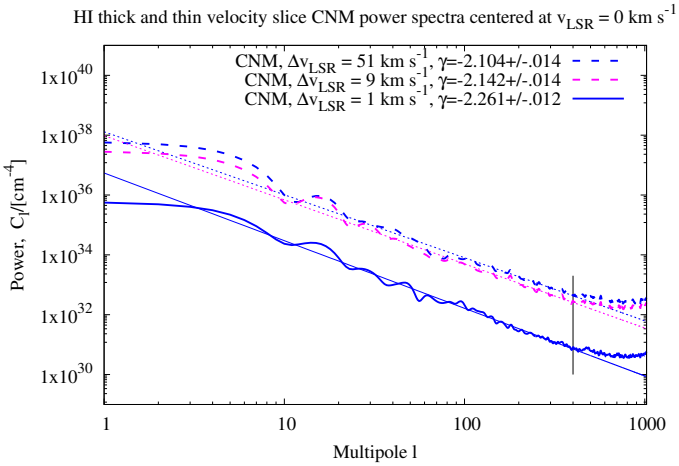


Fig. 3. As in Fig. 1, but for power spectra of the CNM column density distribution at $v_{\rm LSR} = 0$ km s^{-1} for $\Delta v_{\rm LSR} = 1.29$ km s^{-1} (blue solid), $-25 < v_{\rm LSR} < 25$ km s^{-1} (blue dashed), and $-4 < v_{\rm LSR} < 4$ km s^{-1} (magenta dashed). Power spectra were fit for $10 < l < 400$.

Clark et al. (2019) argue that dust is correlated best with cold H I filaments. If their arguments are valid, we expect power spectra for the cold H I to be in better agreement with Fig. 2 than the spectra from Fig. 1. To derive the power distribution of the cold H I we use Gaussian components for the CNM from Kalberla & Haud (2018) and Kalberla & Haud (2019) and repeat the calculation of the thin and thick slice power spectra for the CNM. The results are given in Fig. 3. Comparing the multiphase power spectra from Fig. 1 with Fig. 3 we find that the CNM power spectra are shallower. The power is significantly reduced, but at multipoles $l \gtrsim 400$ there is a strong excess. The implication is that the H I distribution on large scales (low multipoles) is dominated by warm gas, while the CNM controls small scales, as claimed by Clark et al. (2019). The small-scale power excess is strongest for the thin slice power spectrum. We also note that we observe at intermediate multipoles $10 < l \lesssim 400$ a steeper CNM power spectrum in the case of the thin slice, opposite to VCA expectations (Lazarian & Pogosyan 2000, Sect. 4.3). Similar results were reported by Kalberla & Haud (2019). These authors demonstrate that the power excess at high multipoles for HI4PI observations is not affected by noise or instrumental uncertainties. To test whether the same conditions apply to our current data analysis we calculate for comparison a CNM power spectrum for an intermediate channel width of $-4 < v_{\rm LSR} < 4$ km s^{-1}. Comparing this case with the thick velocity slice for $-25 < v_{\rm LSR} < 25$ km s^{-1}, we find only slight changes in the power spectra caused by the source distribution. The CNM has

most of its power at velocities close to zero. There is a slight steepening, but no significant change in the power excess for $l \gtrsim 400$. If this excess had been caused by uncertainties in the data analysis, we should notice an increase of a factor of 5.7 (or $\log(5.7) = 0.75$), corresponding to the decrease in channel width. This is not observed.

The filamentary USM structures used by Clark et al. (2019) are strongly velocity dependent, we therefore expect that power spectra for cold gas should also show some velocity dependences. To check, whether γ is velocity dependent, we calculate single-channel power spectra for $-25 < v_{\rm LSR} < 25$ km s^{-1} for observed multiphase H I column densities and also for the CNM. The spectral indices are displayed in Fig. 4. We find fluctuations up to $\delta\gamma \lesssim 0.5$ in the case of the multiphase H I and $\delta\gamma \lesssim 1$ in the case of the CNM. The velocity dependences are large compared to $\delta\gamma_{\rm VCA} = 0.08$ from Fig. 1.

Figure 4 shows three local minima in γ. The multiphase spectral index is steepest at $v_{\rm LSR} = 1$ km s^{-1} and the CNM power index has a local minimum at $v_{\rm LSR} = 0$ km s^{-1}. The second multiphase local minimum occurs at $v_{\rm LSR} = -6$ km s^{-1}. The thin slice power spectrum for the CNM is steepest at this velocity, but still shallower than the multiphase. Significant fluctuations of the thin velocity slice spectral index with velocity are not expected for the multiphase H I in the VCA framework. Moreover, the changes in spectral index are driven by the CNM and we shall see in Sect. 6 that these fluctuations are associated with changing anisotropies (Fig. 9). The question arises whether VCA is applicable under such conditions.

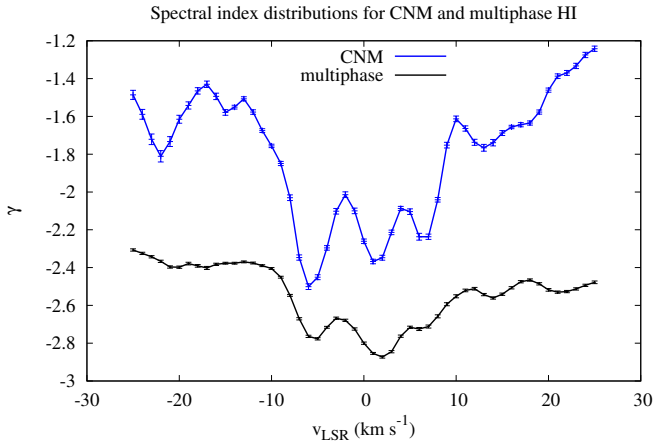


Fig. 4. Velocity dependent single-channel power indices γ for the multiphase H I (black) and for the CNM (blue) with formal 1σ error bars for the fit.

Next we check the VCA key prediction that the spectral index should gradually steepen with the transition from thin to thick velocity slices. A slice is considered to be thick for a width of $\Delta v_{\rm LSR} \gtrsim 17$ km s^{-1}, as expected for warm H I at a Mach number of 1 (Lazarian & Pogosyan 2000, Sect. 4.3). We calculate power spectra in slices with $1.26 < \Delta v_{\rm LSR} \lesssim 51$ km s^{-1}, a range that should cover the transition from thin to thick velocity slices well. In theory, the VCA predicted spectral steepening with velocity width should be independent of the center velocity. Observed velocity dependences of the thin slices from Fig. 4 may imply that such dependences can also affect the VCA and we intend to check possible dependences of this kind. We use two of the prominent local minima from Fig. 4 with $v_{\rm LSR} = 0$ km s^{-1}, and $v_{\rm LSR} = -6$ km s^{-1}. Figure 5 displays the VCA results for the CNM alone and for the observed multiphase H I.

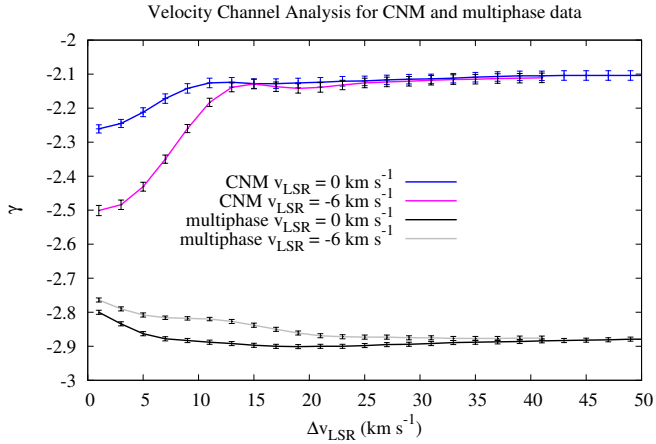


Fig. 5. Velocity dependent single-channel power indices γ for the multiphase H I (black) and for the CNM (blue) with formal 1σ error bars for the fit.

For the multiphase H I with a center velocity $v_{\rm LSR} = 0$ km s^{-1} we see in Fig. 5 that the steepest spectral index is reached at $\Delta v_{\rm LSR} \sim 17$ km s^{-1} but for the very wide range $\Delta v_{\rm LSR} \gtrsim 17$ km s^{-1} the power spectrum appears to flatten again. In the case of a center velocity $v_{\rm LSR} = -6$ km s^{-1} the steepening is somewhat stronger, but still not as significant as predicted by VCA. The result for the CNM clearly indicates that VCA is not applicable in this case. The spectral index flattens progressively with increasing $\Delta v_{\rm LSR}$. The velocity dependences, shown in Fig. 4, dominate in any case the VCA statistics for the cold H I. We show in Fig. 3 that most of the CNM power is concentrated at low velocities. The implication is that the surface filling factor for the CNM is largest at these velocities with a dominance of small-scale structures, as visible in Fig. 4.

We conclude that the objections by Clark et al. (2019) against VCA are justified. Spectral steepening cannot be explained as a decreasing contribution of the velocity field, but rather as a shallower power spectrum for the cold gas in a narrow velocity range. Thus, changes in spectral index must be caused by temperature fluctuations, indicative for phase transitions.

4. Doppler temperatures

In this section we discuss the second key question of whether H I filaments are cold, as claimed by Clark et al. (2019). Filamentary structures discussed by Clark et al. (2014, 2015) are derived by unsharp masking. Low spatial frequencies are suppressed by this method, but the calculations are done independently for each channel, hence velocity dependences of the data (or correlations in velocity) remain unaltered. A priori, a USM treatment should disclose small-scale structure in the observed H I distribution regardless of whether the observed gas is cold or warm. In other words, USM data should show fluctuations in the CNM and in the WNM at high spatial frequencies.

For each USM structure we determine the linewidth and the corresponding Doppler temperature $T_{\rm D}$ as described by Kalberla et al. (2016). Alternatively, we use the CNM Gaussian parameters from Kalberla & Haud (2019) to calculate $T_{\rm D}$, which is an upper limit to the exitation or spin temperature of the H I. In both cases $T_{\rm D}$ has, as expected for a turbulent medium (Vazquez-

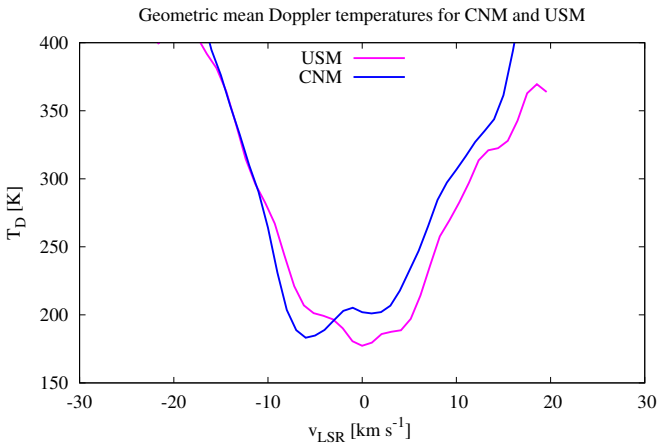


Fig. 6. EBHIS harmonic mean Doppler temperatures, determined from small-scale USM structures and for the CNM from a Gaussian decomposition. USM data for $v_{\rm LSR} > 20$ km s^{-1} are excluded because of their low significance.

Semadeni 1994), a log-normal distribution (e.g., Kalberla et al. 2016, Fig. 13) and we determine independently for each channel of the USM and CNM data the characteristic harmonic mean Doppler temperature, see Fig. 6 for the results.

Even though the selection criteria and numerical methods are very different for the determination of USM and CNM structures, we find good agreement for both independent $T_{\rm D}$ measures. A visual inspection of the data cubes confirms that USM filaments are associated with the CNM, these filaments are always located within CNM structures. USM filaments with Doppler temperatures belonging to the LNM or WNM temperature regimes have never been observed, though unsharp masking was extensively used for quality control of survey data observed with the Effelsberg and Parkes telescopes.

A comparison between Figs. 6 and 4 shows that the local minima in γ, corresponding to steeper spectral indices, are associated with cold H I filaments. The $T_{\rm D}$ curve for the USM data shows bumps that coincide with the local minima in γ. The agreement is less good for the CNM $T_{\rm D}$ curve. We conclude that cold H I small-scale structures are responsible for the observed steepening of thin slice spectral indices. As discussed before, these structures dominate the power spectra at low velocities. Cold small-scale structures may be considered as markers for phase transitions characterized by rapidly reducing kinetic energy with decreasing physical size scale (Wareing et al. 2019). Doppler temperatures $T_{\rm D} \lesssim 200$ K for the region discussed here are exceptionally low. The all sky HI4PI median temperature is $T_{\rm D} \sim 223$ K (Kalberla et al. 2016) and $T_{\rm D} \sim 220$ K was found for the Arecibo sky (Clark et al. 2014). An inspection of Kalberla & Haud (2018, Figs. 9, 10, and 13) indicates that there is cold gas in this region. Peek & Clark (2019) used Na I absorption at high Galactic latitudes to demonstrate that small-scale structures are colder than the environment.

Our results support Clark et al. (2019), and are in clear conflict with Yuen et al. (2019) who deny the existence of cold H I gas in the observed region. This section further supports the conjecture that a steepening of the spectral indices is found for particular cold H I gas condensations on small scales.

5. CNM related to multiphase H I

The CNM is part of the multiphase H I and there appears to be some consensus that these CNM structures are restricted to small scale structures that are embedded in the multiphase H I (e.g. McKee & Ostriker (1977) and Wolfire et al. (2003)). Recent all-sky surveys, like the combined Effelsberg and Parkes H I survey (HI4PI, HI4PI Collaboration et al. 2016) or the Galactic Arecibo L-Band Feed Array Survey (GALFA-H I, Peek et al. 2018) have shown that many or most of the CNM structures need to be considered as part of extended large-scale filamentary structures that are associated with polarized dust emission (Clark, & Hensley 2019).

Fig. 4 rises the question what kind of H I structures might be responsible for the spectral index changes at velocities around $v_{\rm LSR} = -6$, 1, and 6 km s^{-1}. The average H I emission across the the field of view is smooth and without any structures that could resemble fluctuations in Fig. 4 (see Clark et al. 2019, Fig. 1). Power spectra are however affected by emission fluctuations rather than by the average emission and it was shown already in early H I absorption line studies that rms emission fluctuations are related to the line widths of the corresponding CNM absorption lines (Lazareff (1975) and Mebold et al. (1982)). These authors proposed an explanation in terms of turbulence. Mebold et al. (1982) interpret these features as arising in predominantly atomic neutral shells around molecular hydrogen and dust clouds.

In Sect. 4 we discussed the proposal that steep power spectra are related to low Doppler temperatures. The implication would be that velocity channels with low γ values are dominated by H I emission from cold small scale structures with a lot of fluctuations on all scales. To verify this proposal we compare in Fig. 7 the total multiphase H I emission with the CNM emission as derived from our Gaussian analysis. For a better visualization of weak small scale structures we zoom in to the central unapodized region of our field of view, we clip also a part of the strongest multiphase emission structures. Fig. 7 shows on top channel maps at $v_{\rm LSR} = -15$, +15, and -6 km s^{-1}, below at 5, 6, and 7 km s^{-1}. In case of $v_{\rm LSR} = -15$ km s^{-1} the multiphase emission is mostly diffuse but contains some CNM structures. For $v_{\rm LSR} = +15$ km s^{-1} the emission is in general very weak. The case $v_{\rm LSR} = -6$ km s^{-1} is very different with strong emission for multiphase H I as well CNM over most of the field of view. These structures are very complex and require detailed investigations using different intensity windows for different parts of the field. We investigated also the channel map at $v_{\rm LSR} = 1$ km s^{-1}, the situations is there even more complex. We don't show these data and skip also a detailed discussion of the $v_{\rm LSR} = -6$ km s^{-1} to avoid an unnecessary lengthy presentation. At bottom of Fig. 7 we present data for $v_{\rm LSR} = 5$, 6, and 7 km s^{-1}. These figures demonstrate two effects. In the first instance the emission structures change systematically but significantly when incrementing the velocity by only 1 km s^{-1}. It is also obvious from these less crowded fields that most of the CNM structures trace prominent filamentary multiphase H I structures. Many of the CNM structures persist only for three channels, implying a low velocity width or Doppler temperature. Such a FWHM velocity width of 3 km s^{-1} corresponds to a Doppler temperature of $T_{\rm D} \sim 200$ K, a value that was found previously characteristic for filamentary structures (e.g. Clark et al. (2014), Kalberla et al. (2016), and Kalberla et al. (2020)). Several prominent filaments show up with parallel structures for a length of 10°to 20°, resulting in wavy appearance.

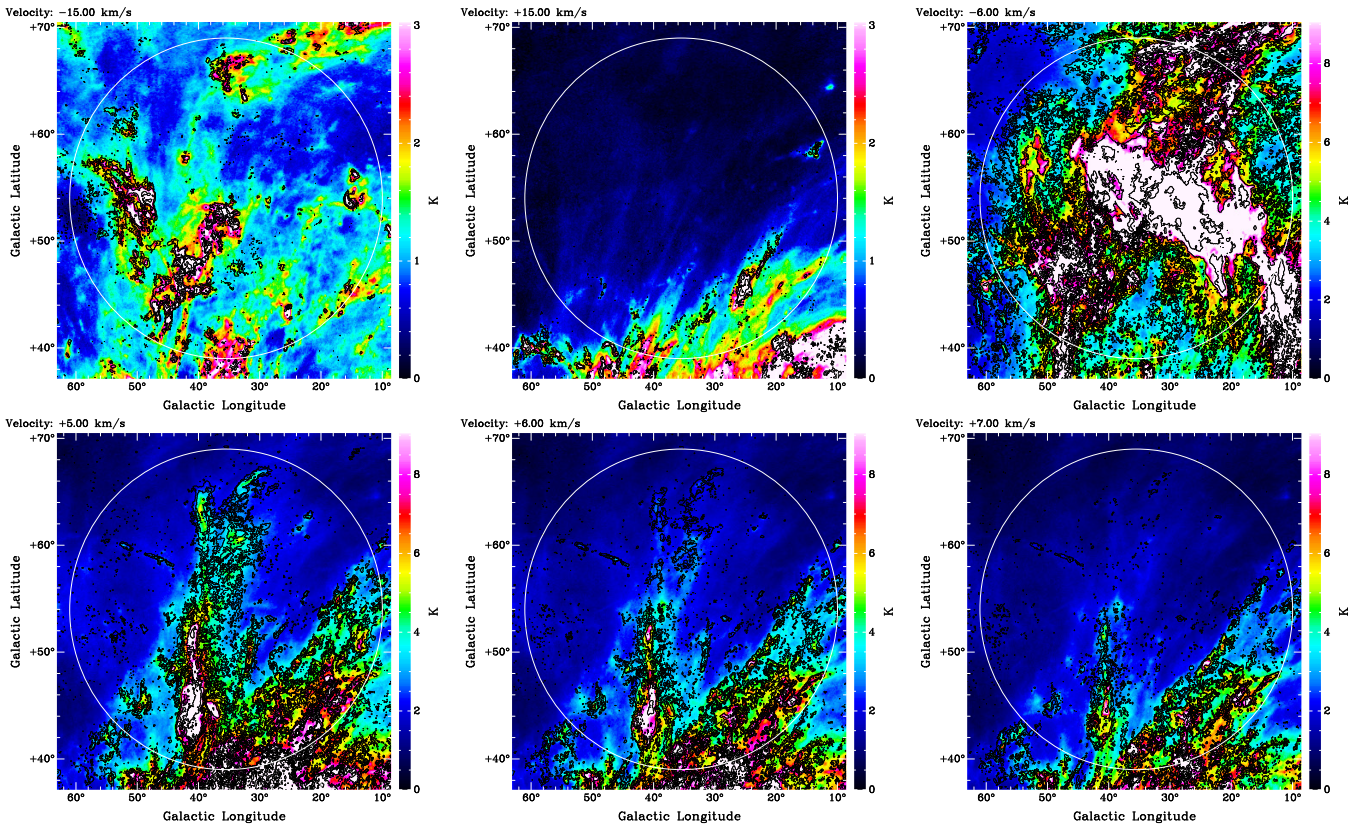


Fig. 7. The distribution of CNM brightness temperatures (isophotes at $T_{\rm B,CNM}$ = 0.3, 1, 3, and 9 K) compared to multiphase brightness temperatures $T_{\rm B}$ (color coded) for the central part of the observed field. We display the distributions at $v_{\rm LSR}$ = −15, +15, and -6 km s^{-1} on top and for $v_{\rm LSR}$ = +5, +6, and +7 km s^{-1} at bottom. These figures may be compared to the CNM structures in the more extended fields in Figs. 9. The circle has a radius of 15°, corresponding to the central unapodized field of view.

Interpreting structures in Fig. 7 we need to take selection criteria into account. Only a fraction of the data can be presented and we have chosen two channels at $v_{\rm LSR}$ = −15 and +15 km s^{-1} as representative for the wings of the γ distribution from Fig. 4. This selection results in multiphase H I structures that contain only a low fraction of CNM with typical line widths of $\Delta v_{\rm LSR} \sim 4$ km s^{-1}. For velocities $-10 \lesssim v_{\rm LSR} \lesssim 8$ km s^{-1} we observe a completely different picture. Except for a diffuse background with $T_{\rm B} \sim 2$ K the H I distribution displayed in the bottom panels of Fig. 7 is dominated by strong CNM emission with low Doppler temperatures. The visual impression of PPV data cubes may be subjective and can be biased by the way the data are presented. We based our selection on results from statistical methods that led to Figs. 4 and 6. These results are objective and unbiased. One may question a relation between spectral index γ (Fig. 4) and harmonic mean Doppler temperature (Fig. 6) but the visual inspection of Fig. 7 supports an interpretation that steep power spectra are caused by particular strong filamentary H I structures that contain significant amounts of CNM with low Doppler temperatures. Cold filamentary or wavy H I structures were previously found to be associated with anisotropies in the power distribution and steep spectral indices (Kalberla & Kerp (2016) and Kalberla et al. (2017)) and these agreements can not be dismissed as purely accidental. It was also shown previously that spectral indices for the CNM depend on the CNM phase fractions (Kalberla & Haud 2019). To verify such dependencies we determine average CNM, LNM, and WNM phase fractions as defined by (Kalberla & Haud 2018) within the inner unapodized field of view with a radius of 15°. These phase fractions are shown in Fig. 8 for comparison with Figs. 4 and 6. Within the velocity range $-8 \lesssim v_{\rm LSR} \lesssim 6$ km s^{-1} most of the the multiphase H I is cold.

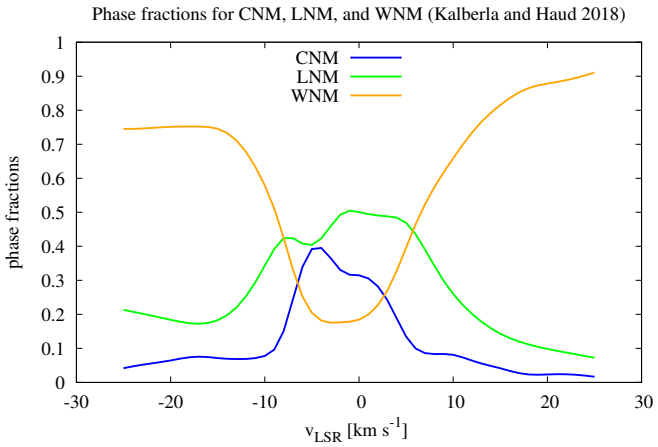


Fig. 8. Velocity distribution of average H I phase fractions for CNM, LNM, and WNM within the inner unapodized field of view with a radius of 15°.

We have chosen for the display in Fig. 7 a lower limit $T_{\rm B}$ = 0.3 K that was used for Gaussian emission structures throughout this analysis. This value corresponds to an approximate three sigma peak noise level; the rms uncertainties for EBHIS amount to 90 mK (HI4PI Collaboration et al. 2016). The analysis of our

Gaussian decomposition algorithm (Haud 2000) with the LDS data, which have similar rms uncertainties of about 80 mK (Hartmann & Burton 1997), has demonstrated that for Gaussians with larger central heights, T_{B0} , our results are in general agreement with the independent decompositions by other authors. The median height of the unmatching Gaussians from different decompositions of the identical profiles was 0.1 K. We analyzed also the dependence of the obtained Gaussians on the observational noise and found that such influence is strongest for Gaussians with $T_{B0} < 0.3$ K. From this we conclude that the Gaussian parameters for the CNM with $T_{B0} \gtrsim 0.3$ K are statistically significant. A general feature of Fig. 7 for all velocities is that small scale CNM structures are in any case embedded in more diffuse multiphase H I structures, as expected from theory (McKee & Ostriker (1977) and Wolfire et al. (2003)).

6. The relation between dust and cold H I gas

The third key question that we like to solve concerns the relation between dust and cold gas. The *Planck* 857 GHz dust emission is dominated by thermal dust and its intensity is proportional to dust column density, which is expected to follow the H I density (Yuen et al. 2019). There appears to be a general consensus that H I gas and dust are frequently filamentary and the FIR emission is closely aligned with prominent USM structures. The debate is whether these filaments indicate cold and dense gas or velocity caustics in a turbulent medium, independent of density and temperature or line width. In the previous section we show that USM structures are on average as cold as the CNM with Doppler temperatures even below 200 K (Fig. 6). Here we explore the spatial relations between FIR, USM, and CNM structures. Clark et al. (2019) demonstrated an increase in the I_{857}/N_{HI} ratio at positions with increasingly stronger USM emission. Such a relation was questioned by Yuen et al. (2019).

The power spectra in Fig. 4 have three well-defined local minima. A visual inspection of the PPV cubes of the USM and CNM emission shows that these extrema are caused by the H I source distribution. We observe three major cloud complexes at velocities $v_{LSR} \sim -6, 0$, and $+6$ km s^{-1}. Depending on velocity, the USM structures are embedded in different CNM structures. This is demonstrated in the upper panels of Fig. 9. The USM structures always follows the CNM. The lower panels show the relation between USM and FIR emission. FIR filaments are associated with distinct USM structures at different velocities and all of the USM channel maps need to be inspected to identify counterparts between FIR and USM data. The H I distribution is very complex, but on visual inspection all of the USM structures at different velocities appear to be related to FIR emission.

For a further numerical analysis of the relation between FIR and H I emission we adopt the hypothesis that all USM structures at all velocities between $-25 < v_{LSR} < 25$ km s^{-1} are associated with dust, hence FIR emission at 857 GHz. We flag the FIR map at all positions with USM emission with brightness temperatures > 0.3 K and replace the observed FIR emission with a constant background level. Following Planck intermediate results XLVIII. (2016) we determined this background level to 1.06 ± 0.16 MJy sr^{-1} within a 12.°5 x 12.°5 field at (GAL= 90°, GAB= −80°) as a 857 GHz FIR background that is unaffected by USM or CNM features; we did not apply any offset corrections for warmer H I components. Figure 10 shows the results after flagging. In the left panel we display for comparison the observed 857 GHz FIR emission, in the middle the FIR after flagging for dust associated with USM structures. After flagging the FIR map for USM signals we repeat the calculations for CNM emission. In the right panel we display the results after flagging for CNM counterparts.

The middle plot of Fig. 10 shows that 83.6% of the FIR emission has been flagged under the assumption that USM and FIR emission are spatially associated. The remaining FIR flux originates close to USM structures, implying that the dust distribution is slightly more diffuse than the USM emission. Inspecting the relation between USM and CNM structures we find that the CNM is in general somewhat more extended than the USM filaments (see Fig. 9 top). FIR emission can be closley linked to the CNM. The result from such a hypothesis is plotted in the right panel of Fig. 10. We find that now 99.6% of the FIR has been flagged. This ratio could be increased by selecting a velocity range of $-30 < v_{LSR} < 25$ km s^{-1}. After a visual inspection of the data we found no indication of dust associated with CNM outside this range. The remaining unflagged positions in Fig. 10 (right; 20% of the observed field) have an average FIR flux density of 1.07 ± 0.18 MJy sr^{-1}, consistent with our previous assumption of a 1.06 MJy sr^{-1} background level. We conclude that a significant fraction of the FIR emission originates from dust that is associated with the CNM. USM structures are spatially embedded within the CNM (see also Fig. 9) and associated with a major part (83.6%) of the dust.

After demonstrating the spatial association between dust and USM structures we want to clarify whether the ratio I_{857}/N_{HI} depends on the strength of the USM intensity, as observed by Clark et al. (2019). These authors used only a fraction of the available data and restricted their analysis to the main H I component close to zero km s^{-1}. Their results were questioned by Yuen et al. (2019), but these authors used only a small 9° x 9° subset of the database. Here we analyze all velocities $-25 < v_{LSR} < 25$ km s^{-1} and the whole field of view. As shown by Fig. 6, the cold gas is concentrated around low velocities; therefore, we integrate the column densities N_{HI} only for velocities in the range $-25 < v_{LSR} < 25$ km s^{-1}. For each position we search for USM emission at all velocities. When we find several USM components at different velocities along the line of sight we assume that these components have the same I_{857}/N_{HI} value. This is an ambiguity in our analysis, but the results do not change if we disregard such positions.

Figure 11 shows histograms for the I_{857}/N_{HI} distributions depending on lower limits T_u for USM intensities. We find that for increasing T_u (thus for more intense USM signals) the I_{857}/N_{HI} distribution shifts to higher values. At the same time we find a significant decrease in the total number of such features. The I_{857}/N_{HI} distribution for $T_u = 0.3$ (all significant USM structures selected) is, as expected for a turbulent medium, approximately log-normal, but this behavior breaks down for higher T_u limits. We calculate the geometric mean and the median for the derived I_{857}/N_{HI} distributions. Figure 12 shows that the mean value for I_{857}/N_{HI} increases continuously with increasing T_u limit. This increase is significant; our results support the findings by Clark et al. (2019); however, as stated by Yuen et al. (2019), the increase in I_{857}/N_{HI} for more pronounced USM structures may be violated in some smaller specific sky patches. Such cases cannot be used as an argument against global and well-defined trends in a turbulent medium.

The H I distribution and in particular the USM structures can be very complex, making the interpretation difficult. Figure 13 shows Renzograms for the field used by Yuen et al. (2019) as the basis for counter-arguments against Clark et al. (2019). Plotted are contour levels for USM intensities of 0.3 K, overplotted for each velocity channel to the FIR distribution in the background. We see here a terribly complicated case with numerous USM

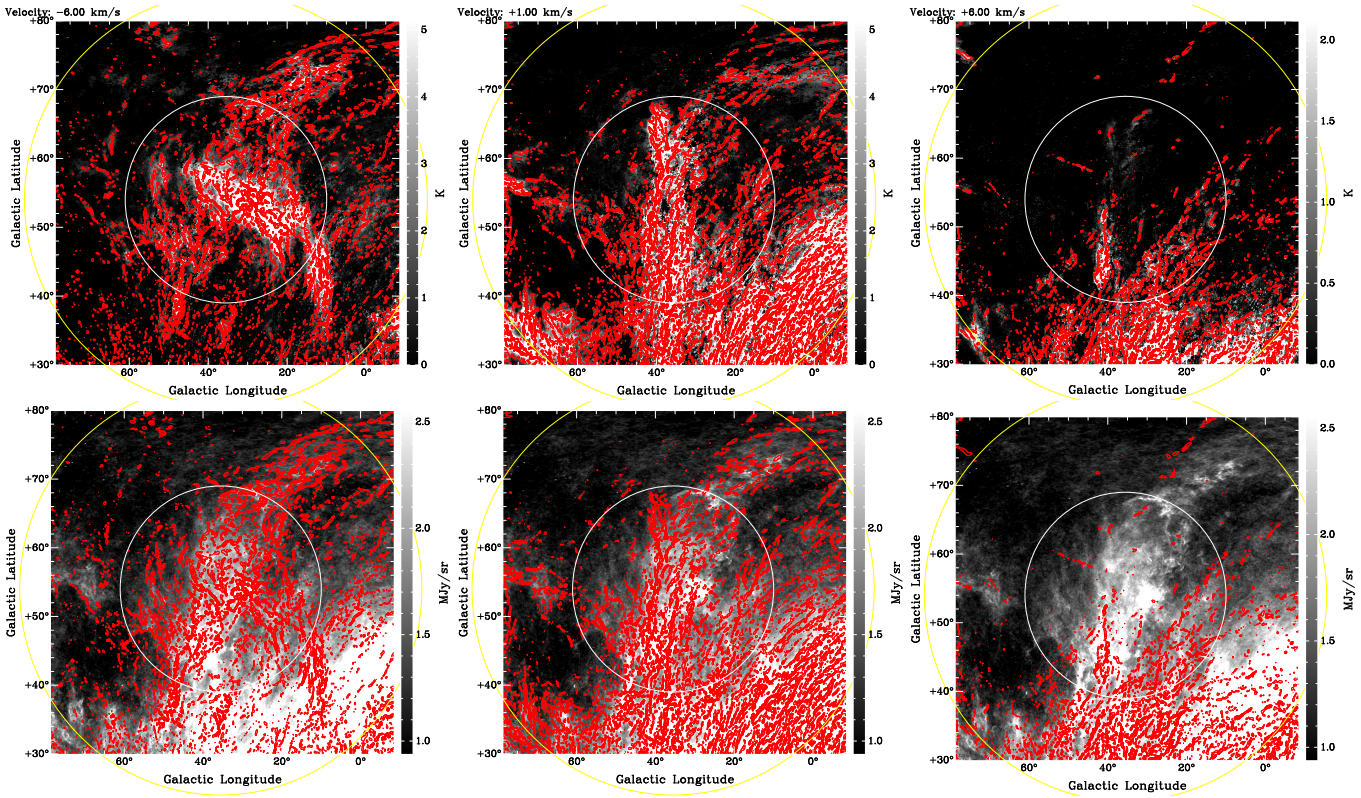


Fig. 9. Upper plots: CNM emission at velocities $v_{\rm LSR} = -6, +1$, and $+6$ km s^{-1} (from left to right), overlayed with red contours from USM emission at the same velocities with a level of > 0.3 K. The lower plots show FIR emission at 857 GHz as observed by *Planck* (left), overlayed with the same USM structures as on top. The circles have radii of 15° (white) and 30° (yellow).

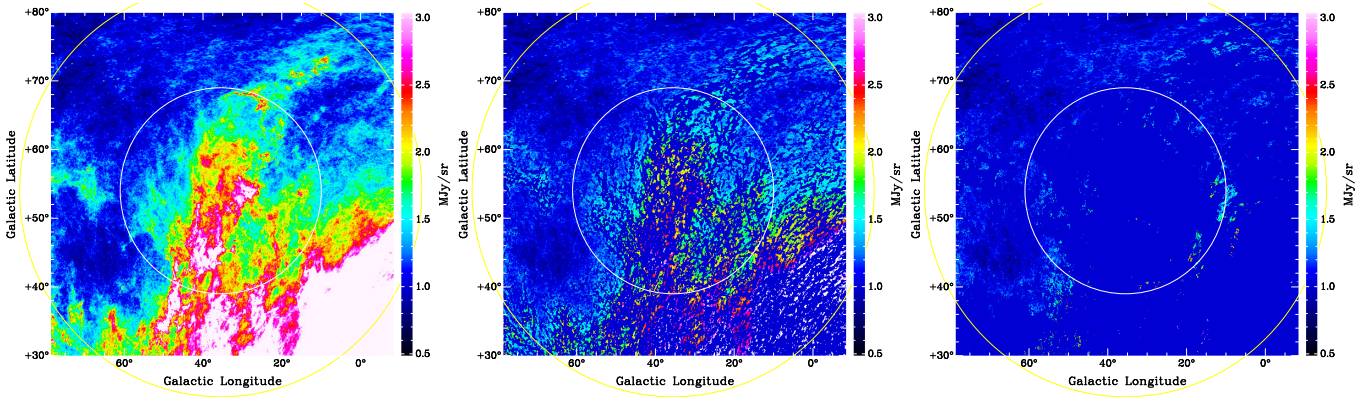


Fig. 10. Far-IR emission at 857 GHz as observed by *Planck* (left), masked in presence of USM structures (middle) and CNM emission (right) at levels of > 3 K. The circles have radii of 15° (white) and 30° (yellow).

worm structures, much more complex than the filamentary USM structures that were considered by Clark et al. (2019, Fig. 8).

7. Discussion

In Sections 3 to 6 we discussed key questions that emerged from the dispute between Clark et al. (2019) and Yuen et al. (2019) about the nature of observed H I structures. We analyzed the same region on the sky as discussed by these authors, but used completely independent data from the EBHIS survey (Winkel et al. 2016). We also used different analysis tools; our intention was to verify the results under discussion. In this section we aim to broaden the discussion, taking particular results from the literature into account that have been neglected so far.

It has been noted by Yuen et al. (2019) that the most valuable insight from Lazarian & Pogosyan (2000) is the prediction of the spectral slope change between the thin and thick PPV slices that is uniquely related to the spectral indices of turbulent velocity and density. A clear support to the VCA predictions was given by Stanimirović & Lazarian (2001), but on the other hand several authors found it difficult to apply VCA for an unambiguous separation of spectral indices between turbulent velocity and density in the Milky Way (Deshpande et al. (2000), Dickey et al. (2001), Miville-Deschênes et al. (2003a,b), Khalil et al. (2006), Roy et al. (2010), Pingel et al. (2018), Kalberla & Kerp (2016), Kalberla et al. (2017), Blagrave et al. (2017), Choudhuri & Roy (2019), and Kalberla & Haud (2019). Many of these authors report that the steepening is restricted to a narrower range in velocity width ($6 \lesssim \Delta v_{\rm LSR} \lesssim 17$ km s^{-1}) than expected ($\Delta v_{\rm LSR} \gtrsim 17$

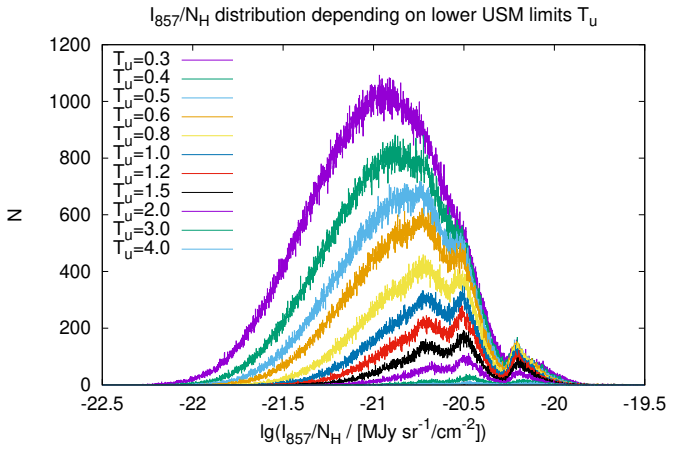


Fig. 11. Histograms for the I_{857}/N_H distributions as a function of the lower limits T_u for the USM emission used to select the data.

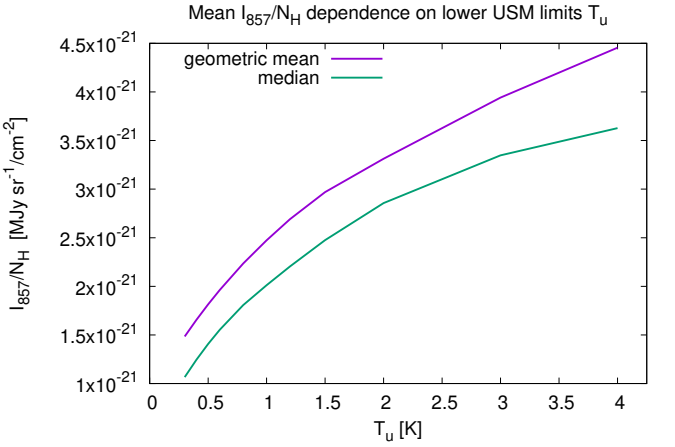


Fig. 12. Dependence of the I_{857}/N_H averages on the lower USM limits T_u used for Fig. 11; shown are geometric mean and median.

km s^{-1}), similar to our finding here. The conclusion is often that there is no significant change in the exponent with the velocity width of the slice. However Yuen et al. (2019, Table 3) redetermine spectral indices for density and velocity and in a few cases draw completely different conclusions from the authors in the original publications of Deshpande et al. (2000), Khalil et al. (2006), and Choudhuri & Roy (2019). Unfortunately neither methods nor reasons for the updates were explained by Yuen et al. (2019), so we need to wait for a further publication of details that can illuminate these discrepancies. It is mandatory to explain what led to such changes. As long as clear statements are missing, the new results in Table 3 of Yuen et al. (2019) remain highly questionable.

A one-to-one relation of changes in spectral slope between thin and thick PPV slices, as predicted by VCA, is hampered by velocity dependences of thin slice spectral indices, as observed by Kalberla & Kerp (2016), Kalberla et al. (2017), Blagrave et al. (2017), Choudhuri & Roy (2019), and Kalberla & Haud (2019). A common finding of these authors is that H I structures in channel maps can change dramatically over even small changes in velocity. Rapid intensity changes with velocity imply in any case a dominance of cold (narrow velocity width) structures. Such changes also affect the power spectra; thin slice spectral indices depend on thermal conditions. Power spectra for the multiphase

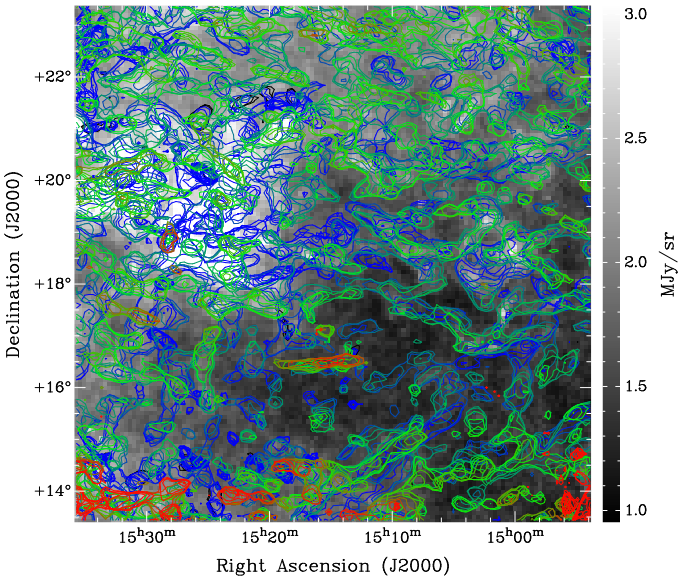


Fig. 13. Renzograms of USM structures in the field discussed by Yuen et al. (2019) at a contour level of 0.3 K; colors represent the velocity field of the USM structures, from negative (blue) to positive (red) radial velocities. The gray scale image in the background shows the FIR emission at 857 GHz.

H I gas steepen as the CNM contribution gets colder, suggesting that the H I phase composition is affecting the turbulent state of the H I. Simulations show that phase transitions cause steep power spectra (Wareing et al. 2019) since thermal instabilities dynamically can form sheets and filaments on typical scales of 0.1–0.3 pc. These simulations show a growth of structures, associated with a rapid rise and steepening of the density power spectra. Our conclusion from Figs. 4 and 6, consistent with the findings of Kalberla & Kerp (2016), Kalberla et al. (2017), and Kalberla & Haud (2019), is that the steepest multiphase power spectra are associated with particularly cold H I gas, observed as CNM and USM structures. Such thin slice power spectra show changes in spectral indices that are far stronger than the observed VCA steepening of the power spectra with velocity width, as proposed by Lazarian & Pogosyan (2000) and Yuen et al. (2019). Our results support the assertion by Clark et al. (2019) that changes in the CNM content predominantly cause the observed fluctuations in spectral indices.

Caustics are caused by geometrical effects; the velocity field can push gas at the same velocity along the line of sight, mimicking density enhancements. Other geometrical considerations may offer an interpretation for the steepening of the power spectra. For optically thin gas, Lazarian & Pogosyan (2000) predict a steepening as the spatial thickness of the analyzed region increases. For a determination of the 3D power-law exponent of the underlying density field the thickness of the sampled region should be at least as large as the dimension of the map perpendicular to the line of sight. In general, it is difficult to estimate the thickness of an observed H I layer; however, applying these considerations to the observed steepening of the H I from Fig. 4 would imply that the depth of the thin slice multiphase H I distribution, as well as the depth of the CNM, would increase at the peak velocities for the spectral indices ($v_{\rm LSR} = -6, 0 + 6$ km s^{-1}). At the same time we observe that this gas is particularly cold (Fig. 6). A similar situation holds for other sources discussed by Kalberla & Kerp (2016) and Kalberla et al. (2017). The conclusion that the extension of H I layers along the line of sight must

be inverse to their Doppler temperatures is so strange that further discussion is not needed.

It was shown by Kalberla & Haud (2019) that the multiphase H I should be considered as a phase composite with CNM, LNM, and WNM. The associated individual power spectra are correlated and differ significantly from the multiphase case. For a complete description it is necessary to take also cross-correlations between these phases into account (Kalberla & Haud 2019, Eq. 4). All of the power spectra for the individual phases are shallow in comparison to the multiphase case with enhanced power for high multipoles. These are spatial frequencies where USM filaments can be observed with large single-dish telescopes. Power spectra for the individual phases at intermediate multipoles $10 \lesssim l \lesssim 100$ are more shallow and for the CNM $\gamma_{\rm CNM} \sim -2.4$ are in far better agreement with $\gamma_{857} \sim -2.5$ than the average multiphase index $\gamma_{\rm NHI} \sim -2.9$. Such an agreement is expected if FIR emission is correlated with CNM and USM structures as proposed by Clark et al. (2019). We show in Sect. 6 that the value of I_{857}/N_{HI} increases with increasing strength of the USM signal. The implication is that either the dust emissivity or dust-to-gas ratio is changed in filaments or that CNM filaments are associated with molecular hydrogen (Clark et al. (2019) and Kalberla et al. (2020)). Optical depth effects have been ruled out by Kalberla & Haud (2019).

Our analysis of the correlation between the FIR emission at 857 GHz and H I structures follows that of Clark et al. (2014) and Kalberla et al. (2016); we use small-scale structures from USM data for correlations with FIR emission. Lazarian & Yuen (2018) identify such filaments in thin channel maps with caustics caused by velocity crowding. Following their assertion, the structures seen in Figs. 9 and 10 need to be interpreted as mere chance coincidences. In addition, the observed dependences between the value of I_{857}/N_{HI} and the strength of the USM signal cannot be explained in this context. We show in Fig. 6 that the USM and CNM structures are both cold, a finding that was also questioned by Yuen et al. (2019). Searching for an interpretation of the I_{857}/N_{HI} ratio in context with the warmer part of the multiphase H I distribution leads to considerable difficulties; we refer to the most recent analysis of the large-scale distribution of interstellar reddening derived from H I emission by Lenz et al. (2017) and further references discussed by these authors. The gas-to-dust ratio is well defined only for $N_{\rm HI} \lesssim 4\ 10^{20}$ cm^{-2} and $E(B-V) \lesssim 0.08$ mag. Figure 9 of Lenz et al. (2017) shows that USM and CNM structures in Figs. 9 and 10 belong to a multiphase medium that is mostly out of this range. Variations in the gas-to-dust ratio are a long-standing problem. Liszt (2014) attributed systematic trends in the gas-to-dust ratio to the onset of H_2 formation at low temperatures. In view of these results our argumentation became circular. Trying to explain the I_{857}/N_{HI} ratio in context with the multiphase H I distribution, we end up with suggestions by Clark et al. (2019), previously rejected by Yuen et al. (2019), that point to the coldest H I components. VCA basically considers a WNM dominated H I fluid at Mach one, and the properties of the embedded CNM are inconsistent with such an approach.

It remains to be explained why the velocity width dependent power spectral indices derived by Stanimirović & Lazarian (2001) are in perfect agreement with the VCA theory by Lazarian & Pogosyan (2000). The derived power spectra come from the observed H I layer of the small Magellanic cloud, extending roughly perpendicular to the line of sight on scales between 30 pc and 4 kpc. In our case, Fig. 3 shows excess power for the CNM at $l \gtrsim 400$, corresponding to scales $\lesssim 0.^{\circ}5$. This corresponds to the angular scale that was used by us to filter USM structures, and corresponds to a linear scale of 1 pc at an assumed distance of 100 pc. Filamentary H I structures were previously reported to have extensions well below a parsec (Clark et al. (2014) and Kalberla et al. (2016)). These are also scales where phase transitions are expected (Audit & Hennebelle (2005), Federrath (2016), and Wareing et al. (2019)). Observations with a beam width of more than 30 times this scale cannot resolve phase fluctuations within the H I layer (imagine what kind of Milky Way ISM research you can do with a 3.3 m dish in place of a 100 m dish). The power analysis for the SMC is sensitive to fluctuations of the total H I column density, to be considered observationally as a single phase only. This is exactly the condition assumed by Lazarian & Pogosyan (2000) and the findings of Stanimirović & Lazarian (2001) provide a direct proof for VCA. In the case of the Galactic H I the single phase assumption is violated and VCA does not apply. The statement by Yuen et al. (2019) that "both two phase and one phase show the same result" is not supported by observations. Fluctuations in spectral indices observed for H I in the Milky Way are predominantly affected by fluctuations in the phase composition. We cannot exclude VCA predicted influences from velocity fluctuations, but these must be marginal compared to changes in spectral index caused by temperature dependences from the CNM. Accordingly velocity caustics must be marginal, and observed filamentary H I structures are caused predominantly by dust-bearing density structures as proposed by (Clark et al. 2019).

8. Summary

Intending to moderate the discussion between Clark et al. (2019) and Yuen et al. (2019) on whether H I filaments are dust-bearing density structures or velocity caustics, we analyzed EBHIS data from the same region around (GAL= $35.^{\circ}5$, GAB= 54°), as used by these authors. We used unsharp masking to determine filamentary H I structures at high spatial frequencies. These structures are cold and associated with FIR emission from dust at 857 GHz. We also used a Gaussian decomposition to extract CNM structures. The USM emission is found to be embedded within the CNM. While the FIR emission is slightly more extended than the USM emission we find that the CNM covers all FIR emission traced by the USM structures. We confirm the results by Clark et al. (2019) that the I_{857}/N_{HI} ratio is elevated in regions with strong USM emission, implying that these structures are density enhancements.

We test the VCA hypothesis that H I filaments originate from velocity caustics, caused by velocity crowding along the line of sight. We calculated the power spectra for the FIR emission, and observed H I column densities and also for the CNM. The single-channel H I power spectra are steepest at velocities where the USM structures and the CNM are coldest. At these velocities the 857 GHz power spectrum ($\gamma_{857} \sim -2.58$) shows the best agreement with the steepest CNM power spectrum ($\gamma_{\rm CNM} \sim -2.5$ at $v_{\rm LSR} = -6$ km s^{-1}). For single-channel power spectra we find power index fluctuations up to $\delta\gamma \lesssim 0.5$ in the case of the multiphase H I and $\delta\gamma \lesssim 1$ in the case of the CNM. These velocity dependences are large compared to the steepening $\delta\gamma_{\rm VCA} = 0.08$ caused by a transition from thin to thick velocity slices. The VCA predicted steepening is marginal in comparison to thin slice index fluctuations that do not exist for an isothermal medium. We find that the spectral index for the multiphase medium is steepest at those velocities where the CNM or USM emission is coldest. Such a coincidence supports an explanation by phase transitions. These lead to a local decrease in the thermal line widths, but the column densities do not change sig-

nificantly. Thus, thermal instabilities produce enhanced power in the line centers of the observed H I at the expense of the power in the wings of the line. Thermal instabilities occur predominantly at small scales, condensations from WNM to CNM thus decrease the multiphase power predominantly at high multipoles. In consequence, the multiphase power spectra steepen, a process that was observed during simulations by Wareing et al. (2019). CNM power spectra are affected in the opposite sense. Phase transition at small scales increase the power at high multipoles, leading to shallower power spectra.

Our results, in agreement with (Clark et al. 2019), call for a significant reassessment of many observational and theoretical studies of turbulence in H I, emphasizing in particular the response from phase transitions. The VCA theory by Lazarian & Pogosyan (2000) is one of the most important contributions to our understanding of the turbulent ISM and has inspired hundreds of publications in this field. The reported discrepancies between theory and observations hamper our understanding of the relations between cold filamentary gas and dust and need urgently be solved.

Comments and discussions in this paper are based on the version of Yuen et al. (2019) as submitted on 5 Apr 2019 to arXiv, available at the time of submission of our contribution. Currently there are 11 citations registered by ADS; the conributions by Yuen et al. (2019) appear to spread out quickly and we would like to argue against theoretical concepts that are opposed by observations.

Acknowledgements. P. K. thanks Jürgen Kerp for support and discussions. U. H. acknowledges the support by the Estonian Research Council grant IUT26-2, and by the European Regional Development Fund (TK133). This research has made use of NASA's Astrophysics Data System. EBHIS is based on observations with the 100-m telescope of the MPIfR (Max-Planck-Institut für Radioastronomie) at Effelsberg. Some of the results in this paper have been derived using the HEALPix package. We also used the Karma package by R.E. Gooch.

References

Armstrong, J. W., Rickett, B. J., & Spangler, S. R. 1995, ApJ, 443, 209
Audit, E., & Hennebelle, P. 2005, A&A, 433, 1
Blagrave, K., Martin, P. G., Joncas, G., et al. 2017, ApJ, 834, 126
Choudhuri, S., & Roy, N. 2019, MNRAS, 483, 3437
Clark, S. E., Peek, J. E. G., & Putman, M. E. 2014, ApJ, 789, 82
Clark, S. E., Hill, J. C., Peek, J. E. G., et al. 2015, Phys. Rev. Lett., 115, 241302
Clark, S. E., Peek, J. E. G., & Miville-Deschênes, M.-A. 2019, ApJ, 874, 171
Clark, S. E., & Hensley, B. S. 2019, ApJ, 887, 136
Dickey, J. M., McClure-Griffiths, N. M., Stanimirović, S., Gaensler, B. M., & Green, A. J. 2001, ApJ, 561, 264
Deshpande, A. A., Dwarakanath, K. S., & Goss, W. M. 2000, ApJ, 543, 227
Federrath, C. 2016, MNRAS, 457, 375
Green, D. A. 1993, MNRAS, 262, 327
Harris, F. J. 1978, IEEE Proceedings, 66, 51
Hartmann, D., & Burton, W. B. 1997, Atlas of Galactic Neutral Hydrogen
Haud, U. 2000, A&A, 364, 83
HI4PI Collaboration, Ben Bekhti, N., Flöer, L., et al. 2016, A&A, 594, A116
Hu, Y., Yuen, K. H., Lazarian, V., et al. 2019, Nature Astronomy, 3, 776
Hu, Y., Yuen, K. H., Lazarian, V., et al. 2019, arXiv e-prints, arXiv:2002.09948v1
Kalberla, P. M. W., Burton, W. B., Hartmann, D. et al. 2005, A&A, 440, 775
Kalberla, P. M. W., Kerp, J., Haud, U., et al. 2016, ApJ, 821, 117
Kalberla, P. M. W., & Kerp, J. 2016, A&A, 595, A37
Kalberla, P. M. W., Kerp, J., Haud, U., & Haverkorn, M. 2017, A&A, 607, A15
Kalberla, P. M. W., & Haud, U. 2018, A&A, 619, A58
Kalberla, P. M. W., & Haud, U. 2019, A&A, 627, A112
Kalberla, P. M. W., Kerp, J., Haud, U. 2020, A&A, in press, arXiv e-prints, arXiv:2004.14630
Khalil, A., Joncas, G., Nekka, F., Kestener, P., & Arneodo, A. 2006, ApJS, 165, 512
Lazareff, B. 1975, A&A, 42, 25
Lazarian, A., & Pogosyan, D. 2000, ApJ, 537, 720
Lazarian, A., & Yuen, K. H. 2018, ApJ, 853, 96
Lenz, D., Hensley, B. S., & Doré, O. 2017, ApJ, 846, 38
Liszt, H. 2014b, ApJ, 783, 17
Martin, P. G., Blagrave, K. P. M., Lockman, F. J., et al. 2015, ApJ, 809, 153
McKee, C. F., & Ostriker, J. P. 1977, ApJ, 218, 148
Miville-Deschênes, M.-A., Joncas, G., Falgarone, E., & Boulanger, F. 2003, A&A, 411, 109
Miville-Deschênes, M.-A., Levrier, F., & Falgarone, E. 2003, ApJ, 593, 831
Miville-Deschênes, M.-A., & Martin, P. G. 2007, A&A, 469, 189
Mebold, U., Winnberg, A., Kalberla, P. M. W., et al. 1982, A&A, 115, 223
Peek, J. E. G., Babler, B. L., Zheng, Y., et al. 2018, ApJS, 234, 2
Peek, J. E. G., & Clark, S. E. 2019, ApJ, 886, L13
Pingel, N. M., Lee, M.-Y., Burkhart, B., & Stanimirović, S. 2018, ApJ, 856, 136
Planck Collaboration, Abergel, A., Ade, P. A. R., et al. 2014, A&A, 566, A55
Planck intermediate results. XXX. 2016, A&A, 586, A133
Planck Collaboration, Aghanim, N., Ashdown, M., et al. 2016, A&A, 596, A109
Planck Collaboration, Akrami, Y., Ashdown, M., et al. 2018, arXiv e-prints, arXiv:1807.06208
Roy, N., Chengalur, J. N., Dutta, P., & Bharadwaj, S. 2010, MNRAS, 404, L45
Roy, N., Minter, A. H., Goss, W. M., Brogan, C. L., & Lazio, T. J. W. 2012, ApJ, 749, 144
Saury, E., Miville-Deschênes, M.-A., Hennebelle, P., Audit, E., & Schmidt, W. 2014, A&A, 567, A16
Schlegel, D. J., Finkbeiner, D. P., & Davis, M. 1998, ApJ, 500, 525
Stanimirovic, S., Staveley-Smith, L., Dickey, J. M., Sault, R. J., & Snowden, S. L. 1999, MNRAS, 302, 417
Stanimirović, S., & Lazarian, A. 2001, ApJ, 551, L53
Vazquez-Semadeni, E. 1994, ApJ, 423, 681
Wareing, C. J., Falle, S. A. E. G., & Pittard, J. M. 2019, MNRAS, 485, 4686
Winkel, B., Kerp, J., Flöer, L., et al. 2016, A&A, 585, A41
Wolfire, M. G., McKee, C. F., Hollenbach, D., & Tielens, A. G. G. M. 2003, ApJ, 587, 278
Yuen, K. H., Hu, Y., Lazarian, A., & Pogosyan, D. 2019, submitted, arXiv:1904.03173

Appendix A: Citations concerning VCA

For the ease of the reader we collect here literal citations that are in conflict with the presentation by Yuen et al. (2019), and parameters as far as their Table 1 is concerned.

Khalil et al. (2006) write in their abstract: "The slopes of the power spectra for an increasing number of velocity channels were compared for 11 sections of the Local arm column density mosaic. All slopes are identical within the uncertainties (-3.0) and we do not detect for the Galactic plane the change in the power law index predicted by Lazarian and Pogosyan." Khalil et al. (2006) give a detailed discussion of these issues in their Sect. 6 and present the results of their VCA analysis in their Tables 3 to 5, also in their Fig. 29. All of these results are in conflict with citations by Yuen et al. (2019) and their Table 1, column 1.

Deshpande et al. (2000) write in their Sect. 5: "In a recent paper, Lazarian & Pogosyan (2000) draw attention to the modification of the H I density spectrum due to the velocity field. They point out that the velocity range needs to be thick in order to obtain the true density power spectrum. They estimate a power-law index close to the Kolmogorov value for the power spectrum of density using the H I emission data of the Galaxy (Green 1993) and of the Small Magellanic Cloud (Stanimirović & Lazarian 2001). Being aware of this complication, we have obtained the power spectra before (case A) and after (case B) averaging in velocity (§4). Within the errors of estimation, the two slopes agree (Fig. 6), indicating that the effect of averaging over velocity is not a substantial effect."

Choudhuri & Roy (2019) write in their abstract: "We also measure the power spectra after smoothing the 21 cm emission to velocity resolution ranging from 1.03 to 13.39 km s^{-1}, but the power spectrum remains unchanged within the error bar." In their Sect. 3 they present in Fig. 7 their data after averaging different velocity channels and conclude: "Clearly, we do not observe any significant difference in the power spectrum after velocity channel averaging. This signifies that the fluctuations are mainly dominated by the density fluctuations."

Appendix B: Related biliographic entries disappear in the arXiv version of a nature paper

After receiving the first referee report on the present paper we resubmitted on 15 February 2020 a revision of our manuscript that was else unpublished at this date. A few days later, on 23 February 2020, the publication by Hu et al. (2019b) appeared as the arXiv version of the original nature astronomy publication (Hu et al. 2019a, 10 June 2019). Whether both events are related to each other is not clear; the coincidence is strange but we may be missing something in this story. Surprisingly, concerning the controversy between Clark et al. (2019) and Yuen et al. (2019), discussed by us in detail, we note some discrepancies between both versions of the Hu et al. publications.

Hu et al. (2019b) state in their Methods section: "The issue of whether the small scale structures in neutral hydrogen velocity channel maps are dominated by density or velocity structures has been debated recently, preprints by Clark et al. (2019)[53] and the response in Yuen et al. (2019)[54]. However, irrespectively of the outcome of these debates, our conclusion that the velocity channel gradients trace magnetic fields well is not affected, especially in the regime of molecular clouds."

While the text is identical in both versions we find in the arXiv version that the nature-style references [53] and [54] are dummies, the original bibliographic entries 53 and 54 are missing and the entries by number refer in Hu et al. (2019b) to completely different unrelated publications. The same happened to references 51 and 52 that refer to the imprint of turbulence on PPV data. Inspecting the arXiv source file shows that in all four cases the modifications were generated through replacing "\cite{...}" by "$^{\color{blue}{...}$". These constructs allow to generate pretended nature-style links to references without the need of existing valid destinations when compiling the source file. In the Hu et al. (2019a) version, published in nature astronomy, all bibliographic entries have valid references.

ArXiv does not care about consistency of the submission. Nature astronomy asks authors to post the submitted version but does not take responsibility for versions on arXiv.